PLOS COMPUTATIONAL BIOLOGY

RESEARCH ARTICLE

# Using deep learning to decipher the impact of telomerase promoter mutations on the dynamic metastatic morpholome

**Andres J. Nevarez, Anusorn Mudla, Sabrina A. Diaz, Nan Hao***

Department of Molecular Biology, School of Biological Sciences, University of California San Diego, La Jolla, California, United States of America

* nhao@ucsd.edu



OPEN ACCESS

**Citation:** Nevarez AJ, Mudla A, Diaz SA, Hao N (2024) Using deep learning to decipher the impact of telomerase promoter mutations on the dynamic metastatic morpholome. PLoS Comput Biol 20(7): e1012271. https://doi.org/10.1371/journal.pcbi.1012271

**Editor:** Kristen M. Naegle, University of Virginia, UNITED STATES OF AMERICA

**Received:** January 22, 2024

**Accepted:** June 22, 2024

**Published:** July 30, 2024



**Data Availability Statement:** The code to reproduce all figures has been deposited in our GitHub repository (https://github.com/dresnevarez/TERTpMut_morpholome). The data is available at (https://zenodo.org/records/11359238).

**Funding:** This work was supported by the following grants and fellowships: A.N. received funding from the Howard Hughes Medical Institute Gilliam Predoctoral Fellowship (https://www.hhmi.org/programs/gilliam-fellows) and the National Academy of Sciences, Engineering, and

## Abstract

Melanoma showcases a complex interplay of genetic alterations and intra- and inter-cellular morphological changes during metastatic transformation. While pivotal, the role of specific mutations in dictating these changes still needs to be fully elucidated. Telomerase promoter mutations (TERTp mutations) significantly influence melanoma's progression, invasiveness, and resistance to various emerging treatments, including chemical inhibitors, telomerase inhibitors, targeted therapy, and immunotherapies. We aim to understand the morphological and phenotypic implications of the two dominant monoallelic TERTp mutations, C228T and C250T, enriched in melanoma metastasis. We developed isogenic clonal cell lines containing the TERTp mutations and utilized dual-color expression reporters steered by the endogenous Telomerase promoter, giving us allelic resolution. This approach allowed us to monitor morpholomic variations induced by these mutations. TERTp mutation-bearing cells exhibited significant morpholome differences from their wild-type counterparts, with increased allele expression patterns, augmented wound-healing rates, and unique spatiotemporal dynamics. Notably, the C250T mutation exerted more pronounced changes in the morpholome than C228T, suggesting a differential role in metastatic potential. Our findings underscore the distinct influence of TERTp mutations on melanoma's cellular architecture and behavior. The C250T mutation may offer a unique morpholomic and systems-driven advantage for metastasis. These insights provide a foundational understanding of how a non-coding mutation in melanoma metastasis affects the system, manifesting in cellular morpholome.

## Author summary

This work explores how specific genetic changes, known as telomerase promoter mutations, influence the shape and behavior of melanoma cells, a highly metastatic and deadly type of skin cancer. These mutations, C228T and C250T, are common in melanoma and are thought to make the cancer more aggressive and metastatic. Cell lines with these

Mathematics Ford Predoctoral Fellowship (https://www.nationalacademies.org/our-work/ford-foundation-fellowships). N.H. received funding from the National Institutes of Health (NIH) under grant numbers R01 GM111458 and R01 GM144595. The funders had no role in study design, data collection and analysis, decision to publish, or preparation of the manuscript. The authors declare no competing interests.

**Competing interests:** The authors have declared that no competing interests exist.

mutations were created, and advanced imaging and deep learning techniques were used to investigate them.

We reveal that cells with the C250T mutation showed more significant cellular morphology and movement changes than cells with the C228T mutation or normal cells. This suggests that the C250T mutation might play a bigger role in helping melanoma spread throughout the body. Detailed changes due to these mutations were visualized and understood using cutting-edge technology to analyze the impact on single cells.

This work is essential because it helps illustrate how tiny genetic changes can lead to significant differences in metastatic behavior. This could lead to better ways to improve early diagnoses and treatment of metastatic melanoma. The findings provide a clearer picture of how melanoma cells evolve and spread, which could guide future cancer research and therapy development.

## Introduction

In the complex world of cellular biology, the interplay between genetic modifications and cellular function is a central theme. The impact of genomic alterations on cellular functions and behavior is undeniably pivotal in the onset and progression of numerous diseases. Genomic alterations, from subtle single nucleotide polymorphisms to extensive chromosomal variations, fundamentally alter cellular function, influencing a cell's ability to survive, replicate, and interact within its environment. Understanding these alterations and their impact on the cellular morpholome is essential for developing novel image-based detection methods, therapeutic strategies, and treatment interventions. Amidst the vast genomic landscape, the promoter region of the telomerase reverse transcriptase (TERT) gene emerges as a significant focal point in melanoma. TERT promoter mutations (TERTp mutations) have been ubiquitously identified across many human cancers, highlighting their critical role in disease progression. In melanoma, these mutations are not mere passengers but active drivers, contributing to melanoma cells' aggressive behavior and metastatic potential [1–4].

Melanoma is a malignant neoplasm arising from melanocytes and is the most aggressive and deadliest form of skin cancer [5]. Despite constituting only about 1% of all skin cancers, melanoma accounts for most skin cancer-related deaths [6]. Over the past several decades, advancements in early detection and an improved understanding of melanoma's molecular mechanisms have contributed to increased survival rates. However, melanoma remains a significant global health concern due to its high propensity for metastasis and resistance to therapies [7]. The metastatic stage of melanoma is primarily responsible for its high lethality, with a 5-year survival rate of only 22.5% for patients with distant metastases [8].

Several genetic and epigenetic alterations have been identified in melanoma that contribute to its aggressive behavior and metastatic potential [1,9,10]. One of the fundamental genetic alterations in melanoma is the presence of mutations in the promoter region of the TERT gene, TERTp mutations–C228T and C250T [11,12]. TERT is a catalytic subunit of the telomerase enzyme, which maintains the telomere length and enables continuous cell division and immortalization [13]. While C228T is generally more frequent than C250T, their prevalence is nearly equal in melanoma compared to other cancer types [14]. TERTp mutations have been found to occur early in melanoma development and become enriched in metastatic tumor sites, suggesting a functional role in the metastatic progression [5].

Melanoma represents an intriguing paradigm of malignancy in cellular morphology and systems biology, where cellular form and function shift dramatically during the metastatic stage. Metastatic melanoma cells undergo a complex and highly regulated process, including

local invasion, intravasation, survival in the circulation, extravasation, and colonization at distant sites [15]. While melanoma's genetic landscape has been extensively explored, understanding how specific genetic mutations influence the cellular architecture and networked systems is essential. The morpholomic implications of these mutations in melanoma metastasis remain poorly understood, and their potential contribution to metastatic phenotypes warrants further investigation.

This hints at TERTp mutations' role in reshaping cellular morpholome, which may be conducive to metastasis. Using quantitative imaging to describe metastatic cellular properties [16], we define the metastatic morpholome as the complete set of single-cell morphological features encompassing dynamic processes such as motility and static measurements such as intensity or deep learned latent features. Recent studies have begun to elucidate the impact of TERTp mutations on melanoma progression, highlighting their influence on various cellular processes, including cell proliferation, migration, and invasion [17,18]. Despite these advancements, a significant limitation lies in the reliance on cancer cell lines or patient-derived tumor samples, which inherently contain many background mutations. These confounding factors potentially obscure the precise effects of TERTp mutations on metastatic phenotypes, necessitating a more isolated and controlled examination.

In response, we meticulously engineer isogenic clonal cell lines with monoallelic TERTp mutations, eliminating the influence of background mutations. This approach allows for a more refined observation of the morpholome implications of these mutations, providing a clearer insight into their role in metastatic behavior. This innovative technique facilitates a comprehensive exploration of the functional clonal consequences of C228T and C250T mutations, offering a detailed understanding of the induced morpholomic variations.

Our findings reveal pronounced morpholomic shifts between cells harboring TERTp mutation variants and their wild-type counterparts. These morpholomic variations encompass diverse aspects, from allele expression patterns to morphological changes, enhanced wound-healing rates, and distinctive spatiotemporal dynamics. A notable observation is the distinct divergence in the influence of C250T and C228T mutations on metastatic phenotypes, countering the previously held belief of their functional equivalence. The C250T mutation demonstrates significant morpholomic shifts, potentially amplifying its metastatic capabilities.

Embracing a symbolic perspective, this work likens the introduction of TERTp mutations to a rock cast into a stream. This seemingly minor mutation sends ripples throughout the cellular morpholome, altering the trajectory and interactions of cellular behavior. This study's design, centered on engineering cells with a non-coding promoter mutation, enables a focused observation and analysis of the mutation's effects on the cellular morpholome. This approach unveils the multifaceted implications of TERTp mutations in melanoma progression and metastasis, offering a novel and enriched perspective on the intricate interplay of genetic modifications and the morpholome. Raw data and code to recreate the figures and analysis are available at the links in our Methods section.

## Results

### C250T correlates with increased metastatic potential and penetrance in multiple organs

A clonal composition change in cancer progression from primary to metastatic disease enriches cells harboring the TERTp mutations [5]. This clonal evolution suggests a functional advantage for metastatic potential and penetrance due to TERTp mutation status. To quantify metastatic potential and penetrance of TERTp mutations *in vivo*, we mined the large-scale pan-cancer study MetMap [19]. MetMap does not include the TERTp mutation statuses of

their cell lines; instead, we searched cell databases and primary literature to identify the TERTp mutation statuses of cell lines. We acknowledge that the size of our C228T and C250T samples used in the subsequent analysis is far from the 500 human cancer cell lines used in the MetMap study because we are limited by the fact that TERTp mutation status can only be found using whole genome or Sanger sequencing. Clinics and research groups often use exome sequencing for cancer mutation profiling. We could not stratify C250T and C228T by cancer type due to a lack of TERTp mutation information for many of the 500 cell lines used in the MetMap study. However, we did find that C250T had higher penetrance and potential than the C228T pan-cancer in all organs (Fig 1A and 1G). Breaking down metastatic potential and penetrance by each organ for TERTp mutations, we see that C250T has significantly higher penetrance in the lungs, liver, and brain (Fig 1B, 1C and 1D). At the same time, the kidney and bone show no difference (Fig 1E and 1F). In addition, C250T has significantly higher metastatic potential in the lung and liver compared to the kidney, bone, and brain, which show no difference (Fig 1H–1L). We found that TERTp mutations do not correlate with aneuploidy, mutational burden, or replication rate of the samples used from the MetMap data.

It should be noted that the difference in the metastatic potential of TERTp mutations in melanoma was corroborated by a recent study using interpretable deep-learned models to identify high and low-efficiency metastatic melanoma single-cell properties [20]. The previously reported interpretable deep-learned model predicted A375, which harbors the C250T mutation [21], to have increased metastatic potential in a patient-derived mouse model. The landmark metastatic melanoma study confirmed this in the metastatic mouse model [22]. While the consensus is that TERTp mutations, C250T, and C228T are genetically identical, these results suggest they differ *in vivo*. Furthermore, since C250T occurs in higher frequency in melanoma, a cancer type known for its aggressive metastatic stage [23], it may significantly

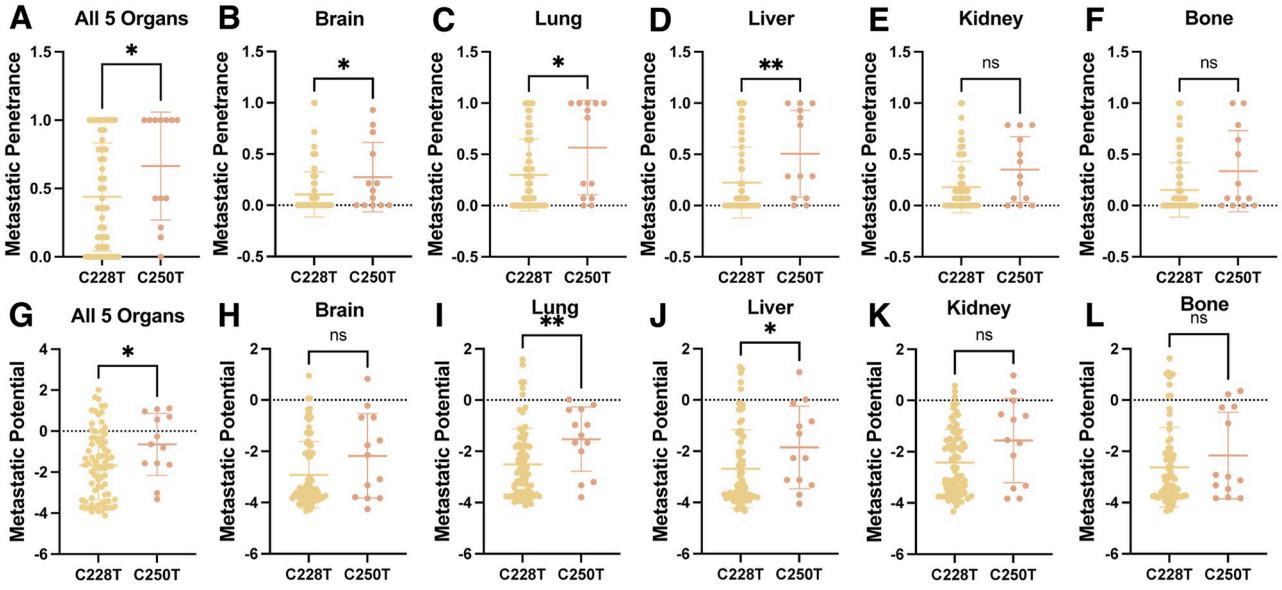


**Fig 1. Analysis of mined information from MetMap database for quantified metastatic potential and penetrance of cell lines harboring Telomerase Promoter Mutations stratified by C228T and C250T.** C228T n = 76, and C250T n = 13. **(A)** Metastatic Penetrance comparison of C228T and C250T aggregated by all organs used in the MetMap database, p = 0.0330. **(B, C, D, E, F)** Metastatic Penetrance comparison of C228T and C250T separated by organ Brain p = 0.0240, Lung p = 0.0326, Liver p = 0.0055, Kidney p = 0.0615, and Bone p = 0.0766. **(G)** Metastatic Potential comparison of C228T and C250T aggregated by all organs used in the MetMap database, p = 0.0326. **(H, I, J, K, L)** Metastatic Potential comparison of C228T and C250T separated by organ Brain p = 0.1555, Lung p = 0.0099, Liver p = 0.0347, Kidney p = 0.0819, and Bone p = 0.3706. All p values from the Mann-Whitney test.

https://doi.org/10.1371/journal.pcbi.1012271.g001

impact metastatic phenotypes. Our meta-analysis shows that pan-cancer tumors harboring the C250T TERTp mutation have higher metastatic potential and penetrance. However, we are not extending this to claim that C250T is solely causative in increasing metastatic potential and penetrance over C228T.

## TERTp mutations increased allele expression, manifesting in multiple changes in cellular properties

To dissect the effect of each TERTp mutation on metastatic relevant cellular properties, we introduced these mutations in HEK 293T cells, which have a minimal mutational burden and unlimited replicative ability due to viral integration rather than TERT mutation or amplification [24]. Since TERTp mutations are mutually exclusive and occur only on one allele, we made individual but not double mutations [12,25]. Importantly, we designed this approach to eliminate potential heterogeneity due to genetics, such as in primary cancer cells or metastatic melanoma cell lines, which would confound our analysis. To this end, HEK 293T $TERT^{WT/WT}$, $TERT^{C228T/WT}$, and $TERT^{C250T/WT}$ single-cell clones were engineered with spectrally distinct fluorescent expression reporters on each allele under the endogenous promoter and at the endogenous loci (Fig 2A and 2B, and S1 Fig). This was meticulously done such that the endogenous TERT promoter controlled the reporters. Furthermore, to preserve the natural genomic context and ensure the native regulatory mechanisms remained intact, these fluorescent reporters were incorporated precisely at the endogenous loci of the TERT gene in the genome; we elected to use P2A [26] so that the expression of the endogenous Telomerase open reading frame is left intact. This setup allowed for an accurate representation of the impact of the respective mutations on gene expression, considering the native chromosomal environment and its potential epigenetic effects. Using quantitative fluorescence microscopy, we observed that the mean expression levels from the TERTp mutation allele increased by ~1.4x over the corresponding WT allele (Fig 2C), consistent with previous studies [25,27–29]. We also observed a significant increase in the mean expression of the C250T over the C228T TERTp mutation allele, which has yet to be reported. We quantified the impact of TERTp mutations on the cell-to-cell variation of allele expression using the Fano Factor (Fig 2D) [30] seen in the single-cell scatter plot (Fig 2E). While both TERTp mutations increased the variations in gene expression relative to WT, and C250T showed a more dramatic effect than C228T.

Building from the unexpected allele expression heterogeneity, we sought to uncover differences in multiple cellular features that define the morpholome, such as intensity, shape, and texture of the cell and nucleus, a total of 523 engineered cell features (S1 Table). We used the CellProfiler Cellpose plug-in to segment the entire cell (S2 Fig) using the phase contrast channel using the Cyto2 model [31,32] to quantify cellular features and a nuclear reporter to get nuclear features. We trained a Random Forest classifier model to discriminate between WT, C228T, and C250T cells using the 523 morpholome features. We found the top features of the Random Forest model related to the expression of the TERTp mutation allele and intensity and texture in the phase contrast image. We plotted the parallel coordinates of the standard deviation of the top 6 normalized features [33] as individual mutation status classes (C228T, C250T, and WT) (Fig 2F) with an accuracy of 67.44% (S3A Fig). We grouped the C228T and C250T mutational status cell lines into a TERTp mutation class (Fig 2H) with an accuracy of 78.50% (S3B Fig).

Following up on the features related to phase contrast images, we trained modified Resnet-50 models to discriminate between WT, C228T, and C250T. We grouped the C228T and C250T mutational status cell lines into a TERTp mutation class [34]. We extracted the latent embeddings of the penultimate layer from the models and used the UMAP dimensionality

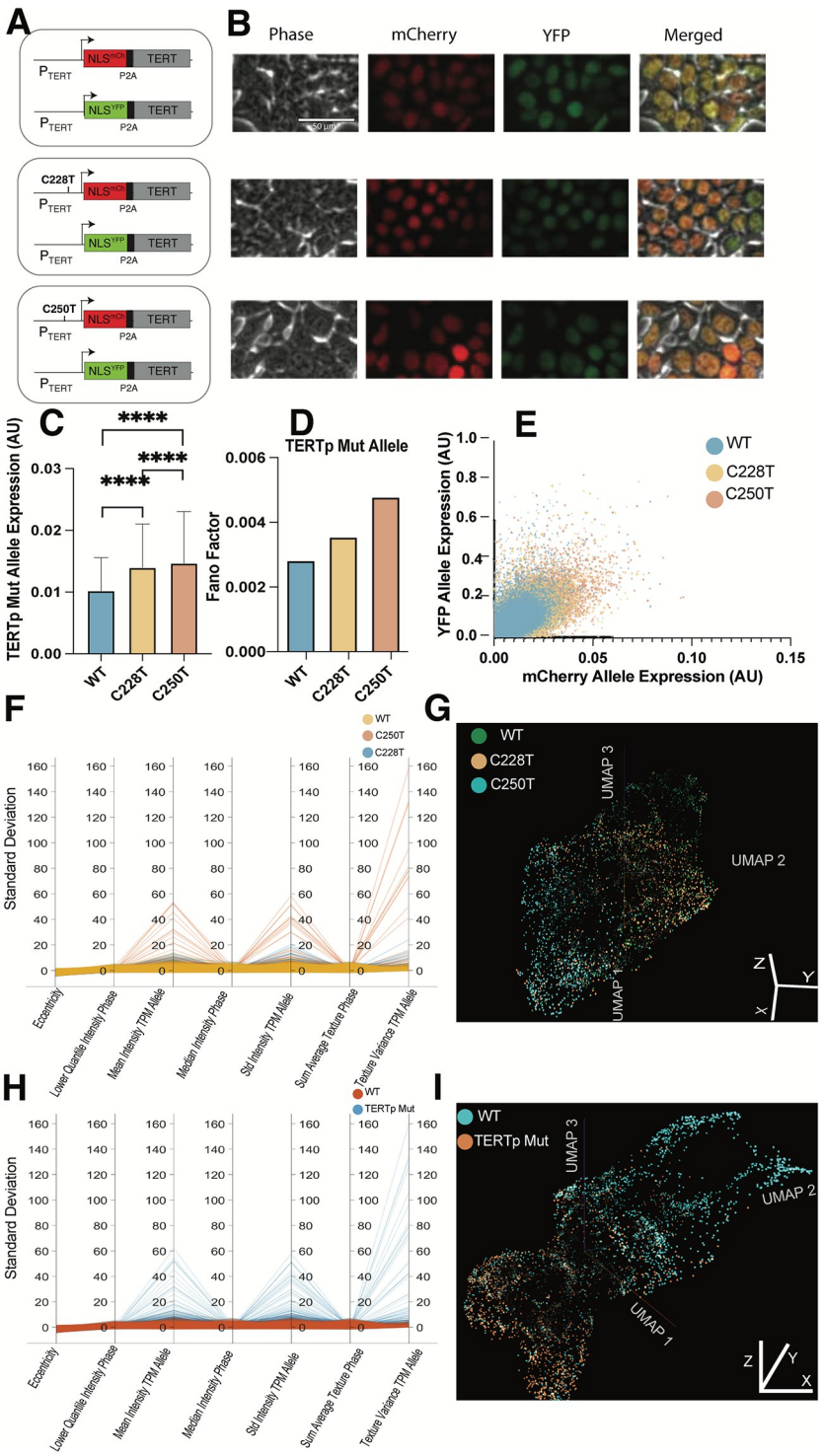


**Fig 2. Introduction of the TERTp mutations illicit a response in the morpholome. (A)** Schematic of the engineered genomic structure of the cell lines. **(B)** False-colored image montage of representative cells for Telomerase promoter mutants, C228T, C250T, and WT cell lines. Telomerase gene expression separated by allele for n = 67,000 cells. **(C)** The bar graph shows the difference in mean mCherry Allele expression of the mutant allele containing the control WT allele and the promoter mutation C228T and C250T, respectively. WT displayed significantly lower expression than C228T $p < 0.0001$ and C250T $< 0.0001$. While C228T showed significantly lower expression than C250T $< 0.0001$ (unpaired t-tests). **(D)** Bar graph showing the allele expression variance for the mCherry Allele quantified using the Fano Factor calculation. **(E)** Scatter plot overlaying the WT, C228T, and C250T allele expression. Each data point

represents a single cell. **(F)** The standard deviation of parallel coordinates of the top 5 discriminative features from a Random Forest trained on individual mutation status features. **(G)** 3D UMAP of the Average Pool 4 latent embeddings in a modified Resnet-50 model trained on phase contrast images labeled by individual mutation status. **(H)** Standard deviation parallel coordinates of the top 5 discriminative features from a Random Forest trained on TERTp mutations (C228T and C250T) and WT features. **(I)** 3D UMAP of the Average Pool 4 latent embeddings in a modified Resnet-50 model trained on phase contrast images labeled by TERTp mutations (C228T and C250T) and WT.

https://doi.org/10.1371/journal.pcbi.1012271.g002

reduction [35] to project these features in three dimensions as individual mutation status classes (C228T, C250T, and WT) (Fig 2G and S1 Movie) and grouped the C228T and C250T mutational status cell lines into a TERTp mutation class (Fig 2I and S2 Movie). The TERTp mutations vs WT model achieved significantly better accuracy than the individual mutation status classes.

## Defining the impact of TERTp mutations on the morpholome

We sought a different experimental modality to highlight cell appearance changes in a non-2D cell culture environment. Imaging Flow Cytometry (IFC) allows the cells to be suspended in solution, experiencing different mechanical properties, which increases the Epithelial to mesenchymal transition (EMT) genes [36]. The increased expression in these pathways may illicit a more pronounced response in cell morphology. The pairing of deep learning and machine learning with IFC has been used to interrogate the metastatic stage in primary samples as part of the pathology pipeline. IFC can probe the cell using cell light scatter and brightfield images. Both require no labels and have been used for cancer classification with deep and machine learning [34,37–39].

Here, we leverage the power of the ImageStream imaging flow cytometry platform [40] and Deepometry [34] to identify differences between WT cells and cells harboring the TERTp mutations and further subtle differences between cells harboring C228T and C250T. We found that we can discriminate between the three cell lines using label-free images alone (S4A Fig). We first examined the latent embeddings of the penultimate layer before the classification grouping the cell lines as TERTp mutation harboring cells vs. WT cells reducing the dimensions using 3D UMAP (S4B Fig, S3 Movie) and 3D PHATE [41] (Fig 3A and S4 Movie) plots for trained model has an overall accuracy of 94.4% (S4C Fig). We observe two clusters of cells in the UMAP plot, showcasing that the TERTp mutations correlate with system-wide changes manifesting in the brightfield and side-scatter images. The PHATE reduction of the same latent embeddings allows us to visualize transition morphological states from WT to TERTp mutations. The clustering suggests that TERTp Mut cells substantially diverge from their WT counterparts regarding cellular morphology. To further understand the transition between WT and TERTp mutant cells, we utilized diffusion pseudotime analysis (Fig 3B). This plot illustrates the continuous trajectory of cell state transitions from WT to TERTp Mutant cells. The progression is color-coded, with blue indicating WT cells and green/yellow representing TERTp Mut cells. The pseudotime trajectory highlights a smooth, gradual morpholomic transition, suggesting the existence of intermediate states during the cellular transformation. This analysis provides insights into the dynamic processes underlying the morphological changes induced by TERT promoter mutations.

Following this, we performed a PAGA (Partition-based graph abstraction) network analysis (Fig 3C), illustrating the connectivity and pseudotime trajectories between different cell clusters. In this network, light blue nodes correspond to WT cells, and orange nodes represent TERTp Mut cells. Thicker edges indicate more robust connectivity, mapping the transition paths and the relationship between distinct cellular states. The PAGA network underscores

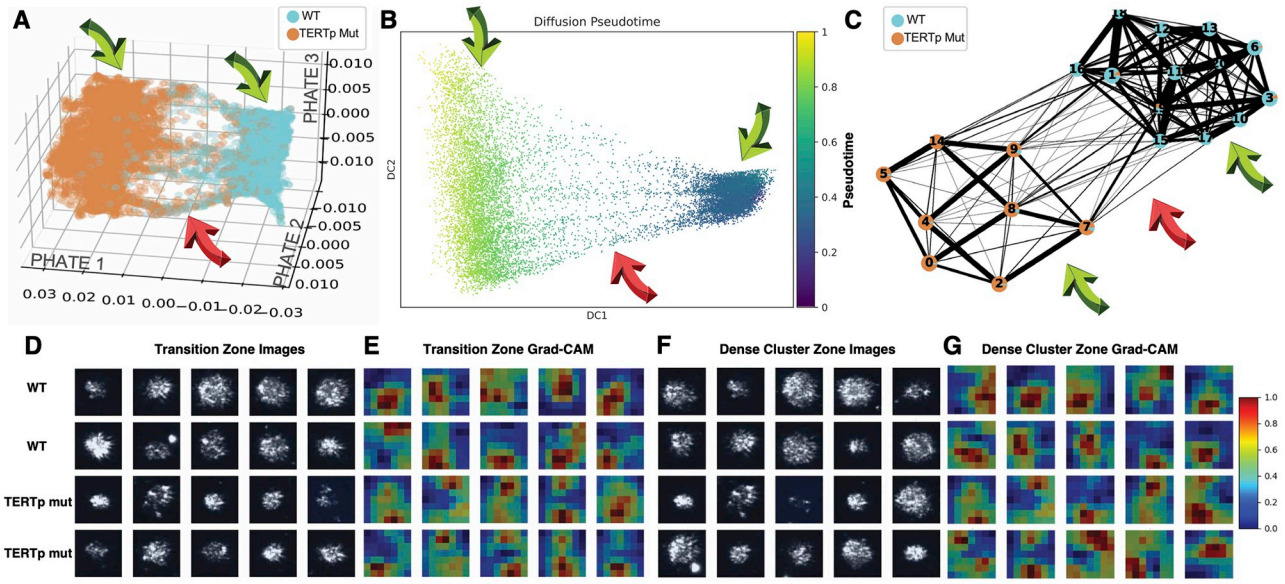


**Fig 3. Analysis of WT and TERTp Mut Cells Using PHATE, Diffusion Pseudotime, and Grad-CAM Visualizations.** (A) PHATE map showing the distribution of wild-type (WT) cells (light blue) and TERT promoter mutant (TERTp Mut) cells (orange). The map illustrates the separation and clustering of the two cell types based on their morpholomic features. (B) Diffusion pseudotime plot indicates WT cells' progression (blue) transitioning into TERTp Mut cells (green). The plot provides a continuous trajectory of cellular differentiation over pseudotime. (C) PAGA (Partition-based graph abstraction) network illustrating the connectivity and pseudotime trajectories between different cell clusters. Light blue nodes represent WT cells, orange nodes represent TERTp Mut cells and pie charts represent WT and TPM proportions. Thicker edges indicate more robust connectivity. (D) Representative images from the transition zone for WT and TERTp Mut cells. The images are organized by cell type, with WT cells in the top two rows and TERTp Mut cells in the bottom. These images highlight the morphological changes occurring in the transition zone. (E) Grad-CAM (Gradient-weighted Class Activation Mapping) heatmaps for transition zone images, highlighting regions of interest in the cell images that are most relevant for distinguishing between WT and TERTp Mut cells. The color scale ranges from blue (low relevance) to red (high relevance). (F) Representative images from the dense cluster zone for WT and TERTp Mut cells. These images show the cells in more stable and distinct morphological states. (G) Grad-CAM heatmaps for dense cluster zone images, showing regions of significant changes between WT and TERTp Mut cells. The heatmaps emphasize areas within the cells that exhibit notable differences in texture and intensity.

https://doi.org/10.1371/journal.pcbi.1012271.g003

cell states' structured progression and branching, offering a detailed view of the cellular dynamics and transitions induced by TERT promoter mutations. Some WT and TERTp mutant cells exist in both clusters, albeit at different proportions. Each node depicts (pie chart) each node's composition (WT or TERTp mutant), showing low distributions and clarifying the specifics of the overlap and transitions not seen in the PHATE and pseudo time plots. The pseudotime analysis and PHATE reduction show that WT cells occupy a smaller morpholomic space with less variance than the TERTp mutated cells, corroborating our findings (Fig 2D and 2E).

We sought to characterize morphological transition (red arrows) through representative images. We display representative images from the transition zone for WT and TERTp Mut cells. These images are organized by cell type, with WT cells depicted in the top two rows and TERTp Mut cells in the bottom two rows. The transition zone images highlight the morphological variations and transitional states between WT and mutant cells (Fig 3D). These visual representations are crucial for understanding the specific changes in cell morphology associated with TERT promoter mutations. To identify the regions of morphological significance within the transition zone images, we employed Grad-CAM (Gradient-weighted Class Activation Mapping) analysis, as shown in (Fig 3E). These heatmaps highlight regions within the cell images that are most relevant for distinguishing between WT and TERTp Mut cells. The color scale ranges from blue (indicating low relevance) to red (indicating high relevance), with

significant regions marked in red. This analysis reveals the crucial morphological features impacted by TERT promoter mutations and visually represents the areas within the cells that contribute most to their classification. Based on the Grad-CAM analysis, we see that the brightfield images per cell offer a low impact on the classification decision (S4D Fig). Therefore, we only show the SSC images in our montage.

To uncover the differences between the dense cluster zones (green arrows). Representative images from the dense cluster zone for WT and TERTp Mut cells (Fig 3F) depict cells in more stable and distinct morphological states, reinforcing the divergence observed in the PHATE and pseudotime analyses. The dense cluster zone images provide a clear contrast between the WT and TERTp Mut cells, highlighting the stable morphological characteristics of each cell type. We present Grad-CAM heatmaps for the dense cluster zone images (Fig 3G), showing regions of significant changes between WT and TERTp Mut cells. These heatmaps emphasize areas within the cells that exhibit notable differences in texture and intensity, further delineating the morphological impacts of TERT promoter mutations. The Grad-CAM analysis in the dense cluster zone corroborates the findings from the transition zone, providing additional evidence of the significant morphological alterations induced by TERT promoter mutations.

Next, we trained a model grouping the mutation statuses individually with an accuracy of 62.4% (S4E Fig). We still observe two distinct clusters in the 3D UMAP (S4G Fig, S5 Movie); however, C250T and C228T do not cluster individually within the supercluster. We visualize the latent features using PHATE (S4F Fig, S6 Movie) and observe the transition states in granular detail. Similar to the UMAP, there are two clusters of cells, with one cluster predominantly related to WT, while the other corresponds to the C228T and C250T features.

These techniques allow us to delineate the impact of the TERTp mutations on the morpholome. Additionally, we trained a Random Forest Classifier on the quantified engineered cell features; we achieved an accuracy of 94% (S5A Fig) with the top features relating to image morphology, particularly texture, intracellular light scattering (intensity), and sub-cellular spatial distribution differences (radial distribution of Zernike features) (S5B Fig). Still, size was not different between TERTp mutations and WT. Combining these three techniques, we can confidently say the differences in morpholomic profiles between TERTp mutations and WT cells are related to changes in texture and intensity features.

## TERTp mutations increase wound healing spatiotemporal migration dynamics

Following up on our findings from Fig 1 regarding C250T increasing penetrance *in vivo*, we wanted to investigate if C250T increases collective cell migration using the wound healing assay. Wounds are a breach in cells that are usually linked tightly to each other to form a protective barrier and are suddenly separated. Similarly, cells detach from their neighbors in metastasis and adopt a migratory behavior to reach new locations. The wound repair program is suspected of equipping both types of cells to survive this anchorless state [42]. This allows cells to move into the breach and make new tissues, enabling metastatic cells to detach and colonize new destinations. Increased Telomerase expression has been shown to promote the epithelial-to-mesenchymal transition and three-dimensional invasion through Matrigel *in vitro* [43,44]. The close connection between the telomerase and WNT/β-catenin pathways is connected to invasiveness and stemness in cancer [43,45,46].

We investigated the spatiotemporal dynamics of collective cell migration between the three clonal cell lines via in vitro wound healing using previously published software. The WT cell line had a significantly lower healing rate than C228T and C250T. C250T showed a substantially higher healing rate than C228T (Fig 4A). The overall distances migrated showed similar

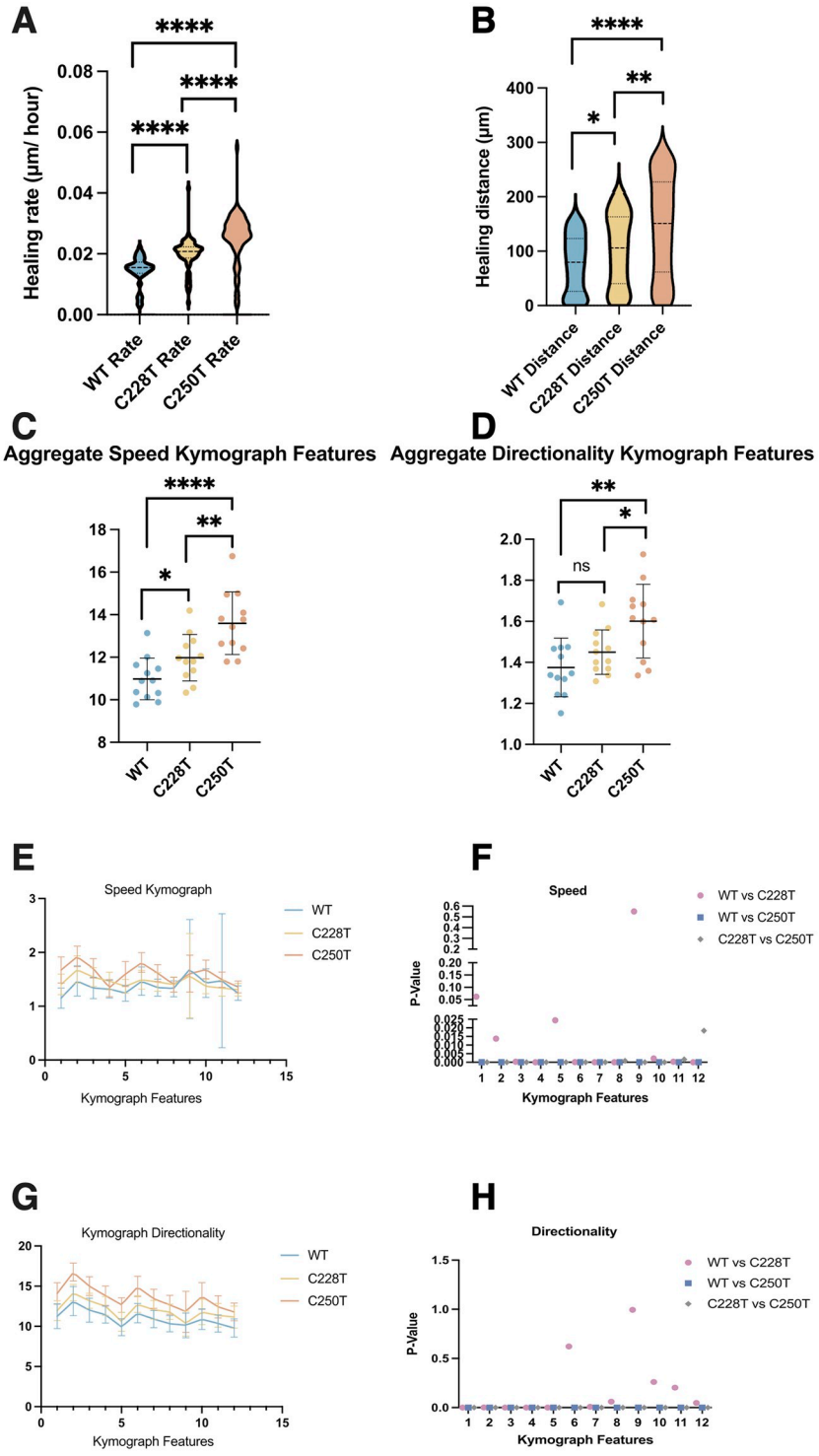


**Fig 4. C250T has increased spatiotemporal monolayer migration using live-cell *in vitro* wound-healing assay.** n = 38 movies for each cell line. **(A)** Violin plot comparison of healing rates across cell lines. WT compared to C228T p <0.0001, WT compared to C250T p <0.0001, and C250T compared to C228T p <0.0001. **(B)** Total distance in microns is the leading edge covered throughout the movies. WT compared to C228T p = 0.0175, WT compared to C250T p = 0.0047, and C250T compared to C228T p <0.0001. Aggregate comparisons of the average of each of the 12 kymograph features for all movies across cell lines. **(C)** Speed of each of the 12 averaged figures. WT compared to C228T p = 0.1600, WT compared to C250T p = 0.0036, and C250T compared to C228T p = 0.0332. **(D)** Directionality of each of the 12 averaged figures. WT compared to C228T p = 0.0242, WT compared to C250T p <0.0001, and C250T

compared to C228T p = 0.0083. **(E)** Graph showing the speed of individual 12 kymographs features averaged among the 38 movies with SD error bars. **(F)** Graph depicting p-values from multiple Mann-Whitney tests for speed features. WT compared to C228T were significantly different in features 2–8 and 10–12 with p values 0.013734, 0.000344, 0.000010, 0.024413, 0.000085, 0.000010, <0.000001 and 0.002214, 0.000359, and 0.000014 respectively. Features 1 and 9 were not significantly different, with p-values of 0.061604 and 0.550616, respectively. WT compared to C250T were significantly different in all 12 features, p <0.000001. C228T compared to C250T differed substantially in all features with corresponding p values of <0.000001, <0.000001, <0.000001, 0.000012, <0.000001, <0.000001, 0.000006, 0.000887, 0.000008, 0.000003, 0.001708, 0.018402. **(G)** Graph showing the directionality of individual 12 kymographs features averaged among the 38 movies with SD error bars. **(H)** WT compared to C228T differed significantly in directionality features 1–5 and 7 with p values <0.000001, 0.001646, 0.000027, 0.000670, 0.000093, and 0.008123 respectively. While features 6 and 8–12 were not significantly different with corresponding p values of 0.621746, 0.060135, 0.993789, 0.260206, 0.203475, and 0.048283. WT compared to C250T were significantly different in all 12 features, p <0.000001. C228T compared to C250T differed significantly in all 12 features p <0.000001. All p values from Mann-Whitney tests.

https://doi.org/10.1371/journal.pcbi.1012271.g004

patterns, with WT having significantly lower spaces than C228T and C250T. In contrast, C250T migrated further than C228T (Fig 4B).

We also examined the averaged speed and directionality of the kymographs across experiments. We found that C228T showed a significantly higher speed than WT but a very modest difference in directionality compared to WT. C250T, however, showed substantially higher speed and directionality than either WT or C228T (Fig 4C and 4D). We then investigated the speed in each of the 12 features of the kymographs individually. We found that WT and C228T differed in only six features, whereas C250T showed significant differences in all 12 features compared to WT or C228T (Fig 4E and 4F). We next examined the speed of each of the 12 features. C228T displayed significant differences from WT in 10/12 features, whereas C250T differed from WT or C228T in all 12 features (Fig 4G and 4H).

We showed that C250T has a considerable advantage in terms of healing rate and overall distance covered in an *in vitro* wound-healing assay, followed by C228T and WT. Furthermore, C250T has notable spatiotemporal differences in speed and directionality propagating from the wound edge into the monolayer compared to WT and C228T. C228T lags behind C250T in all metrics but is still significantly faster and migrated further than WT, with significant spatiotemporal differences in nearly all 12 features. These results align with the differences observed in TERT expression from C228T and C250T (Fig 2), which may underlie the higher metastatic potential and penetrance of C250T compared to C228T (Fig 1).

## Discussion

While the reactivation of Telomerase is crucial for melanoma development, there is no direct link between long telomeres and metastatic potential [47] in melanoma. This suggests that, besides enabling replicative immortality, Telomerase may have alternative functions [48] relevant to withstanding cellular stress during metastasis. TERTp mutations are enriched in metastatic tumors across various cancer types, signifying a stereotypical advantage in surviving cellular stress for disseminating cells. Although both C228T and C250T TERTp mutations generate a new *de novo* Erythroblast Transformation Specific (ETS) transcriptional binding site, their prevalence differs across cancers, with C228T being predominant, except in melanoma [12]. Metastatic melanoma exhibits high metastatic potential and is linked to changes in morphological cellular properties [20]. However, the specific metastatic relevant cellular morpholome properties affected by TERTp mutations remain undefined.

TERTp mutations are associated with changes in cellular morphology. Telomerase reverse transcriptase is traditionally associated with its role in telomere lengthening and chromosomal stability, but its expression in melanoma cells has broader implications for cancer progression.

Increased TERT expression has been linked to more efficient early metastasis [49], as it plays a part in the invasion-metastasis cascade, which includes several steps from local invasion to distant colonization. TERT may influence the local invasion of primary melanoma cells through its impact on cellular programs, such as NF-kB and metalloproteinases [44, 50], beyond its canonical telomerase activity. Furthermore, gene expression analyses have revealed that TERT expression is co-regulated with integrins, TGF-beta, and interleukins [51]. This suggests that TERT may contribute to remodeling the extracellular matrix, a critical process that drives cancer stemness, supports cancer cell invasion and requires morphological dynamic changes.

Furthermore, TERTp mutations increase Keratins and extracellular matrix proteins. Keratin KRT17 is a critical structural component of the cytoskeleton, providing cell protection and support [52]. KRT17 is notably overexpressed in various cancers, including gastric, cervical, oral squamous cell carcinoma, and breast cancer [53–57] with TERTp mutations. Extracellular matrix protein 1 (ECM1) is another significant molecule. This glycoprotein plays roles in cell proliferation, angiogenesis, migration, and metastasis [58,59]. Elevated ECM1 expression has been observed in several cancers, such as thyroid, gastric, colorectal, and lung carcinoma, invasive ductal breast carcinomas, hepatocellular cancer, and more. Notably, a significant increase in ECM1 expression is seen in malignant epithelial tumors, particularly those with distant metastases. Understanding the multifaceted role of TERTp mutations in these cellular processes could provide new insights into therapeutic targets for cancer treatment.

This study uses live cell imaging, machine learning, and deep learning to investigate how TERTp mutations influence metastatic relevant cellular morpholome properties. We first exploited the extensive database of quantified *in vivo* metastatic fitness in MetMap, revealing through meta-analysis that tumors with C250T TERTp mutation have increased metastatic potential and penetrance across all studied organs than those with C228T TERTp mutation (Fig 1). While the two TERTp mutations are regarded as genetically identical, their differential impacts *in vivo* suggest an underlying divergence in function. Notably, the heightened prevalence of the C250T mutation in aggressive metastatic melanomas underscores the significant clinical implications of this mutation in tumor progression and metastasis. Having established *in vivo* differences, we sought to observe the morpholome differences.

To understand the effect of TERTp mutations on the morpholome without the confounding influence of mutations and copy number variance, we engineered isogenic cell lines containing C228T or C250T TERTp mutations at the endogenous locus under the endogenous promoter to examine the impact of TERTp mutations *in vitro*. C250T confers increased expression and variance of TERT expression than C228T. C250T has higher levels of variance in the top discriminative features of our Random Forest model than C228T. Stochastic gene expression allows clonal populations to exhibit phenotypic heterogeneity, possibly aiding in metastatic dissemination [60–63]. We posit that the increase in the heterogeneity of TERT expression could be a barrier to effective therapy [64], which might account for the metastatic cell's ability to survive multiple stressors in metastatic dissemination. Moreover, using machine-learned models based on over 500 cell features, we could distinguish between C250T and C228T with high accuracy and low false positives (Fig 2). Interpreting the top discriminative features of the model further elucidated the morpholomic differences induced by these TERTp mutations.

To further understand cell morphology in a non-2D culture, we used a different live cell imaging modality, Imaging Flow Cytometry (IFC). Using the IFC modality, we have delineated morphological differences between these isogenic cell lines, which differ in only one base pair. Using label-free images (SSC and Brightfield) to define the morpholome alone was sufficient to distinguish these cell types, suggesting profound morphological changes induced by the TERTp mutations (Fig 3). Nonetheless, discerning between the two TERTp mutations,

C228T and C250T, remains challenging, indicating the subtle differences between these mutations. However, we visualized the trajectory from WT to TERTp mutations and the discriminatory feature patterns of the deep-learned model using GradCam, allowing us to interpret what cellular properties changed: texture and intracellular intensity or light-scattering properties. We can accurately discriminate between TERTp mutations and WT cells, meaning the latent embeddings of TERTp mutations are stereotypical image features of TERTp mutation-related metastasis. While C228T is more common in patients, the C250T has the plasticity to transition back and forth, supporting the increased *in vivo* fitness (Fig 1). This illustrates how a non-coding mutation affects the single-cell system beyond the increase in gene expression. While considerable work remains to translate this to clinical pipelines, these results show the capability of label-free morphological features to identify cells harboring TERTp mutations and direct treatment plans.

We sought to understand how these static morpholome profiles held up during dynamic processes, such as migration, which is critical to metastasis. Cells with the C250T mutation displayed increased migration rate, distance traveled, coordination, and speed at the leading edge and throughout the monolayer, likely mirroring their increased metastatic abilities *in vivo*. Furthermore, the spatiotemporal dynamics between the cell types followed the same trend we have seen in our other results, with C250T having the most increased migration dynamics, followed by C228T and then the WT cells. The intricate interplay between the TERTp mutations and the wound repair machinery, especially given the role in facilitating metastatic dissemination, is intriguing. Our results hint at the potential therapeutic relevance of targeting the wound repair pathways in cancers harboring TERTp mutations (Fig 4). It has recently been shown that when there is cell crowding (monolayer), ETS variant 4 (ETV4) expression increases [65], which connects monolayer migration to gene expression. Meanwhile, the TERTp mutations create a new ETS site. Our monolayer migration wound healing experiments show a preferential increase of TERTp mutation C250T. This furthers the link between TERTp mutation expression and the mechanical and morphological dynamics.

In the evolving landscape of metastatic research, understanding metastasis's genetic and morpholomic underpinnings is pivotal. Our study sheds light on the functional impact of TERTp mutations on morpholome cellular properties related to metastatic potential, cellular expression, and migration dynamics. Though our analysis clearly shows increased robustness in C250T-bearing cells, it is vital to note that we are not purporting that the mutation is the sole causative factor to metastatic potential, but rather, how it affects the cellular system as readout from the morpholome. Our research underscores the multifaceted impacts of TERTp mutations, notably C250T, in promoting metastatic potential, altering gene expression dynamics, and inducing distinct cellular phenotypes. While we have charted new territories in understanding the differential *in vitro* roles of TERTp mutations, further exploration into their mechanistic underpinnings will be instrumental in devising novel therapeutic interventions for TERTp mutation-bearing cancers. Given the ever-important proper screening of biopsy samples, we envision developing morpholome-based AI models based on imaging flow cytometers like the Amnis ImageStream [40], BD S8 with Cellview [66], and Deepcell's REM-I system [67] to provide a metastatic potential score that associates with the increased potential derived from the TERTp mutations.

## Materials and methods

### Cell culture and origin

HEK293T was ordered from ATCC (ATCC CRL-11268) and tested negative for Mycoplasma using a Mycoplasma detection kit (Southern Biotech). HEK293T cells were cultured in

Dulbecco minimal essential medium (DMEM: Thermo Scientific HyClone #SH30022FS) supplemented with 10% fetal bovine serum, four mM L-glutamine, 100 I.U./ml penicillin, and 100 mg/ml streptomycin at 37 ˚C, 5% CO2 and 90% humidity.

## Transfection

The transfections were performed with a 1 mg DNA: 2 ml Fugene HD (Promega E2311) ratio. Cells were seeded at 300,000 cells/well in a six-well plate for 18 hours before transfection. Two days after transfection, puromycin was added to the medium at 1 mg/ml, and cells were selected for two days. Survival cells were grown for another seven days before being sorted with FACS into 96-well and expanded into monoclonal cell lines. We plated 300,000 cells/well in a 6-well plate overnight, then transfected with 1.25 ug gRNA and 1.25 ug linearized donor with 5 ul FugeneHD in 100 ul final volume in Opti-MEM.

## Construct designs and homogenous clonal cell line creation

We followed the CRISPR/Cas9 protocol [68] to construct the reporter cell line. In general, the gRNAs were designed by the online CRISPR tool (http://crispr.mit.edu), and the DNA oligos were ordered from Eurofins Genomics, annealed, and cloned into pSpCas9(BB) P2A-Puro (Addgene #48139) vector plasmids. gRNA plasmids were transfected into HEK293T cells and tested for gRNA efficiency using the T7 endonuclease assay. Only the most efficient gRNA was used with the donor DNA. The donor plasmids were constructed using the Gibson assembly method. We used site-directed in-vitro mutagenesis to make a synonymous substitution in the donor plasmids to avoid gRNA recognition and Cas9 cutting of the linearized donor DNA. We first developed a nuclear marker cell line by inserting the nuclear localization signal and two copies of infrared fluorescent protein (NLS-2xiRFP) [69] under the endogenous actin promoter. This was followed by a P2A spacer in HEK293T cells. This cell line ensured a constitutive expression without introducing an exogenous strong constitutive promoter and greatly assisted cell segmentation and tracking. Briefly, the gRNA and the linearized donor DNA were transfected into HEK 293T cells, and the transfected cells were screened with 1 mg/ml puromycin for two days. The cells were allowed to grow for an additional five days before being sorted by FACS. The fluorescently positive cells were sorted as single cells into 96-well plates [68]. We collected at least 500 single cells. We grew the cells for an additional three weeks to obtain homogenous clones. On average, about 30% of cells formed colonies, and all were screened for a fluorescent signal with the microscope. A minimum of 10 clones were then genotyped and checked for homozygosity and correct integration using at least three pairs of primers, which were confirmed with sequencing. Positive clones were further validated with a western blot to ensure valid protein expression. After construction and validation, the engineered single-clonal cell line was assigned a unique identification number, entered into our electronic database, and stored in liquid nitrogen with a cryoprotectant. The same procedure was performed for CRISPR-based tagging of the other allele of Telomerase. Cells were screened with puromycin and sorted by FACS to generate monoclonal cell lines.

## Flow cytometry and single-cell sorting

Cells were released via trypsinization and filtered through a cell strainer to create cell populations "cloned" from a single cell (Fischer; 07-201-430). To ensure a single-cell solution, cells were resuspended in HBH and analyzed using a benchtop BD FACSAria Fusion flow cytometer (BD Biosciences, Franklin Lakes, NJ). Single-cell clone generation of WT and TERTp Mutation cell lines were sorted using fluorescent-activated cell Sorting into 96-well plates.

Acquired flow cytometry data were all analyzed using FlowJo software (Tree Star). All cells were gated on FSC, SSC, and iRFP, and then mCherry and YFP took cells from the bulk of the populations, not the outliers. Single cells were identified via phase contrast and fluorescence microscopy. Once confluent within the well, the clonal populations were released via trypsinization, transferred to individual cell culture dishes, and allowed to expand until confluency.

## Live cell imaging

The imaging medium is phenol red-free DMEM (Life Technology-Gibco) with the same supplements as the regular culture medium. Live cell phase contrast and fluorescence imaging were performed on a Nikon Ti microscope with an environmental chamber at 37oC and 5% CO2 in 20x magnification (pixel size of 0.803μm). Cells were seeded in a 24-well polystyrene dish with a cell count of 240,000 cells in 4 mL of phenol-red free DMEM per dish. The dish was then placed in a 37˚C incubator for 24 hours to allow cells to recover from trypsinization before imaging. Snapshot images were taken before the time-lapse. Time-lapse imaging was performed for 3–4 days to allow for multiple cell divisions.

## Collective cell migration

Cells were grown in a 2-well culture insert (ibidi; 81176) until a cell monolayer was established using Phenol-red free DMEM. The insert was removed, and 1ml medium was added while monolayer positions were imaged every 10 minutes over 24 hours. Each time-lapse movie was inspected for quality over 24 hours. If the movie time needed to be cropped due to monolayers colliding, we removed these time frames so as not to affect the analysis; all movies had the same time length: step-by-step instructions and code availability [70]. The plots were generated using PRISM 9. The kymograph methods are from an existing tool from a paper and chapter (Zabary, Y., Zaritsky, A. (2022) and PMID: 28512143). The kymograph analysis was employed to study dynamic cellular processes. Time-lapse microscopy images were acquired at 20-minute intervals using a high-resolution phase-contrast microscope and preprocessed with Matlab to enhance contrast and reduce noise. The kymographs were then analyzed to measure parameters such as velocity, directionality, and movement frequency, with additional quantitative analyses performed using MATLAB.

## Cell segmentation and feature quantification

Background correction was performed using ImageJ's Rolling Ball background subtraction algorithm with a 15-pixel radius [71]. We used Cellpose and CellProfiler [72] to automate cellular and nuclear segmentation using phase images and nuclear iRFP images. We also excluded non-cell objects by size and shape selection. Cell segmentations were then subject to manual inspection, and segmented objects that did not correspond to cells were eliminated. Cells in active replication were removed based on size.

## Deepometry Deep-learning-based model

We used the Matlab version of Deepometry [34] for our multi-channel imaging flow cytometry image dataset. Software links are available in the original manuscript [34]. Deepometry is a framework for applying supervised and weakly supervised deep learning to imaging data with multiple channels. It is developed to prepare imaging data in the proper format for deep learning and carry out phenotype classification. The software is built upon established deep learning architectures, including the modified ResNet-50 architecture.

## UMAP and PHATE Dimensionality reduction

We took the latent embedding output (tsv files) and performed dimensionality reduction (UMAP) using Tensorflow Embedding Projector (https://projector.tensorflow.org). The code for PHATE reduction has been deposited in our GitHub repository.

## Random Forest Model

Our study used the Random Forest model provided by CellProfiler Analyst. This model is a pre-established tool within the software, and we did not modify its underlying architecture or hyperparameters. The specifics of the Random Forest model, including the number of trees, the depth of trees, and other parameters, are within the CellProfiler Analyst software manual and are consistent with the details provided in the latest CellProfiler Analyst documentation.

## Partition-based Graph Abstraction (PAGA)

To delineate the landscape of cell populations and their developmental trajectories, we employed Partition-based Graph Abstraction (PAGA). This method involves clustering cells based on their single-cell morpholomic profiles using the Leiden algorithm, then constructing a graph where nodes represent clusters and edges indicate the presence of significant connectivity between clusters. The abstraction provided by PAGA enables a more precise visualization of the possible paths of cellular differentiation and hierarchies, facilitating the interpretation of complex single-cell data. The code is deposited in our GitHub repository.

## Diffusion Pseudotime Analysis

Diffusion Pseudotime (DPT) was utilized to order cells along a developmental trajectory, quantifying their progression through different biological states. By embedding the single-cell morpholomic data into a diffusion map space, we calculated a pseudotime score for each cell from a random WT root cell, representing a non-cancerous/metastatic state. This analysis helped identify key transitional stages and branching events in the cellular morpholome differentiation. The code is deposited in our GitHub repository.

## Gradient-weighted Class Activation Mapping (Grad-CAM)

For model interpretability, Gradient-weighted Class Activation Mapping (Grad-CAM) was applied. This technique generates a visual explanation for decisions made by the model, highlighting the important regions in the input image that contribute to a specific class prediction. The gradients of the target output concerning the feature maps of a convolutional layer are captured, weighted, and combined to produce a heatmap. This heatmap overlaid on the original image elucidates the model's focus areas, aiding in the validation and refinement of model predictions.

The code is deposited in our GitHub repository.

## Imaging flow cytometry acquisition

Cells were released via trypsinization to image single cells and filtered through a cell strainer (Fischer; 07-201-430). Cells were resuspended in HBH and analyzed using a benchtop ImageStream X platform to capture images of live HEK 293T cells. For each cell, we captured images of brightfield and side scatter images. After image acquisition, we used the IDEAS analysis tool (accompanying the ImageStream X software) to discard multiple cells or debris, omitting them from further analysis. ImageStream settings: Sample volume: 1 ml. Flow

diameter: 7 mm. The velocity of flow: 44 m s 1. Resolution: 0.5 mm. Magnification: 40. Camera sensitivity: 256 on all channels. Camera gain: 1. Brightfield LED intensity: 88 mW. Darkfield laser intensity: 1 mW. 405 nm laser set to 15 mW.

### Quantification and statistical analysis of Metastatic potential and penetrance

The mining of cell databases and primary papers determined TERTp Mutation status. Plots were made in PRISM 9.

### General image analysis

All computations were performed on an AMD Ryzen 5 3600 CPU @ 4.1 GHz machine with an NVIDIA RTX 3060 GPU running Windows 10 Professional. This workstation was built as a moderate deep-learning workstation accessible to most research budgets.

## Supporting information

**S1 Fig. Cell line construction diagram.**
(PNG)

**S2 Fig. Cellpose segmentation example.**
(PDF)

**S3 Fig. Random forest confusion matrices of engineered features.**
(PDF)

**S4 Fig. IFC supplement.**
(PDF)

**S5 Fig. Random Forest IFC supplement.**
(PDF)

**S1 Table. Feature list in reverse importance order.**
(XLSX)

**S1 Movie. 3D UMAP movie of C228T, C250T, and WT.**
(MOV)

**S2 Movie. 3D UMAP movie of TPM and WT.**
(MOV)

**S3 Movie. 3D UMAP movie of TPM and WT.**
(MOV)

**S4 Movie. 3D PHATE movie of TPM and WT.**
(GIF)

**S5 Movie. 3D UMAP movie of C228T, C250T, and WT.**
(MOV)

**S6 Movie. 3D PHATE movie of C228T, C250T, and WT.**
(GIF)

## Acknowledgments

We thank Yishaia Zabary for advising on the Spatiotemporal monolayer migration software parameters. We thank Dr. Phuc Nguyen and Dr. Paula Godoy in the Hao lab for providing feedback on the manuscript.

## Author Contributions

**Conceptualization:** Andres J. Nevarez, Nan Hao.

**Data curation:** Andres J. Nevarez, Anusorn Mudla, Sabrina A. Diaz.

**Formal analysis:** Andres J. Nevarez, Sabrina A. Diaz.

**Funding acquisition:** Andres J. Nevarez, Nan Hao.

**Investigation:** Andres J. Nevarez.

**Methodology:** Andres J. Nevarez.

**Project administration:** Nan Hao.

**Resources:** Andres J. Nevarez, Nan Hao.

**Software:** Andres J. Nevarez.

**Supervision:** Nan Hao.

**Validation:** Andres J. Nevarez.

**Visualization:** Andres J. Nevarez.

**Writing – original draft:** Andres J. Nevarez.

**Writing – review & editing:** Andres J. Nevarez, Anusorn Mudla, Nan Hao.

## References

1. Guo Y, Chen Y, Zhang L, Ma L, Jiang K, Yao G, et al. TERT Promoter Mutations and Telomerase in Melanoma. J Oncol. 2022; 2022:6300329. https://doi.org/10.1155/2022/6300329 PMID: 35903534
2. Nagore E, Rachakonda S, Kumar R. TERT promoter mutations in melanoma survival. Oncotarget. 2019; 10(16):1546–8. https://doi.org/10.18632/oncotarget.26688 PMID: 30899422
3. Hugdahl E, Kalvenes MB, Mannelqvist M, Ladstein RG, Akslen LA. Prognostic impact and concordance of TERT promoter mutation and protein expression in matched primary and metastatic cutaneous melanoma. Br J Cancer. 2018; 118(1):98–105. https://doi.org/10.1038/bjc.2017.384 PMID: 29123258
4. Shaughnessy M, Njauw C-N, Artomov M, Tsao H. Classifying Melanoma by TERT Promoter Mutational Status. Journal of Investigative Dermatology. 2020; 140(2):390–4.e1. https://doi.org/10.1016/j.jid.2019.06.149 PMID: 31425705
5. Griewank KG, Murali R, Puig-Butille JA, Schilling B, Livingstone E, Potrony M, et al. TERT promoter mutation status as an independent prognostic factor in cutaneous melanoma. J Natl Cancer Inst. 2014; 106(9). https://doi.org/10.1093/jnci/dju246 PMID: 25217772
6. Hodis E, Watson IR, Kryukov GV, Arold ST, Imielinski M, Theurillat JP, et al. A landscape of driver mutations in melanoma. Cell. 2012; 150(2):251–63. https://doi.org/10.1016/j.cell.2012.06.024 PMID: 22817889
7. Mattia G, Puglisi R, Ascione B, Malorni W, Carè A, Matarrese P. Cell death-based treatments of melanoma:conventional treatments and new therapeutic strategies. Cell Death & Disease. 2018; 9(2):112. https://doi.org/10.1038/s41419-017-0059-7 PMID: 29371600
8. Sundararajan S, Thida AM, Yadlapati S, Koya S. Metastatic Melanoma. StatPearls. Treasure Island (FL): StatPearls Publishing Copyright © 2023, StatPearls Publishing LLC.; 2023.
9. Seynnaeve B, Lee S, Borah S, Park Y, Pappo A, Kirkwood JM, et al. Genetic and Epigenetic Alterations of TERT Are Associated with Inferior Outcome in Adolescent and Young Adult Patients with Melanoma. Sci Rep. 2017; 7:45704. https://doi.org/10.1038/srep45704 PMID: 28378855

10. Blanco-García L, Ruano Y, Blanco Martínez-Illescas R, Cubo R, Jiménez Sánchez P, Sánchez-Arévalo Lobo VJ, et al. pTERT C250T mutation: A potential biomarker of poor prognosis in metastatic melanoma. Heliyon. 2023; 9(8):e18953. https://doi.org/10.1016/j.heliyon.2023.e18953 PMID: 37609429

11. Horn S, Figl A, Rachakonda PS, Fischer C, Sucker A, Gast A, et al. TERT promoter mutations in familial and sporadic melanoma. Science. 2013; 339(6122):959–61. https://doi.org/10.1126/science.1230062 PMID: 23348503

12. Huang FW, Hodis E, Xu MJ, Kryukov GV, Chin L, Garraway LA. Highly Recurrent TERT Promoter Mutations in Human Melanoma. Science. 2013; 339(6122):957–9. https://doi.org/10.1126/science.1229259 PMID: 23348506

13. Shay JW, Wright WE. Telomeres and telomerase: three decades of progress. Nat Rev Genet. 2019; 20(5):299–309. https://doi.org/10.1038/s41576-019-0099-1 PMID: 30760854

14. Vinagre J, Pinto V, Celestino R, Reis M, Pópulo H, Boaventura P, et al. Telomerase promoter mutations in cancer: an emerging molecular biomarker? Virchows Arch. 2014; 465(2):119–33. https://doi.org/10.1007/s00428-014-1608-4 PMID: 25048572

15. Fares J, Fares MY, Khachfe HH, Salhab HA, Fares Y. Molecular principles of metastasis: a hallmark of cancer revisited. Signal Transduct Target Ther. 2020; 5(1):28. https://doi.org/10.1038/s41392-020-0134-x PMID: 32296047

16. Nevarez AJ, Hao N. Quantitative cell imaging approaches to metastatic state profiling. Frontiers in Cell and Developmental Biology. 2022; 10. https://doi.org/10.3389/fcell.2022.1048630 PMID: 36393865

17. Bell RJ, Rube HT, Kreig A, Mancini A, Fouse SD, Nagarajan RP, et al. The transcription factor GABP selectively binds and activates the mutant TERT promoter in cancer. Science. 2015; 348(6238):1036–9.

18. Stern JL, Paucek RD, Huang FW, Ghandi M, Nwumeh R, Costello JC, et al. Allele-Specific DNA Methylation and Its Interplay with Repressive Histone Marks at Promoter-Mutant TERT Genes. Cell Reports. 2017; 21(13):3700–7. https://doi.org/10.1016/j.celrep.2017.12.001 PMID: 29281820

19. Jin X, Demere Z, Nair K, Ali A, Ferraro GB, Natoli T, et al. A metastasis map of human cancer cell lines. Nature. 2020; 588(7837):331–6. https://doi.org/10.1038/s41586-020-2969-2 PMID: 33299191

20. Zaritsky A, Jamieson AR, Welf ES, Nevarez A, Cillay J, Eskiocak U, et al. Interpretable deep learning uncovers cellular properties in label-free live cell images that are predictive of highly metastatic melanoma. Cell Systems. 2021; 12(7):733–47.e6. https://doi.org/10.1016/j.cels.2021.05.003 PMID: 34077708

21. Heidenreich B, Rachakonda PS, Hemminki K, Kumar R. TERT promoter mutations in cancer development. Curr Opin Genet Dev. 2014; 24:30–7. https://doi.org/10.1016/j.gde.2013.11.005 PMID: 24657534

22. Quintana E, Piskounova E, Shackleton M, Weinberg D, Eskiocak U, Fullen DR, et al. Human Melanoma Metastasis in NSG Mice Correlates with Clinical Outcome in Patients. Science Translational Medicine. 2012; 4(159):159ra49–ra49. https://doi.org/10.1126/scitranslmed.3004599 PMID: 23136044

23. Tracey EH, Vij A. Updates in Melanoma. Dermatologic Clinics. 2019; 37(1):73–82. https://doi.org/10.1016/j.det.2018.08.003 PMID: 30466690

24. DuBridge RB, Tang P, Hsia HC, Leong PM, Miller JH, Calos MP. Analysis of mutation in human cells by using an Epstein-Barr virus shuttle system. Mol Cell Biol. 1987; 7(1):379–87. https://doi.org/10.1128/mcb.7.1.379-387.1987 PMID: 3031469

25. Hafezi F, Perez Bercoff D. The Solo Play of TERT Promoter Mutations. Cells. 2020; 9(3):749. https://doi.org/10.3390/cells9030749 PMID: 32204305

26. Kim JH, Lee S-R, Li L-H, Park H-J, Park J-H, Lee KY, et al. High Cleavage Efficiency of a 2A Peptide Derived from Porcine Teschovirus-1 in Human Cell Lines, Zebrafish and Mice. PLOS ONE. 2011; 6(4):e18556. https://doi.org/10.1371/journal.pone.0018556 PMID: 21602908

27. Huang D-S, Wang Z, He X-J, Diplas BH, Yang R, Killela PJ, et al. Recurrent TERT promoter mutations identified in a large-scale study of multiple tumour types are associated with increased TERT expression and telomerase activation. European Journal of Cancer. 2015; 51(8):969–76. https://doi.org/10.1016/j.ejca.2015.03.010 PMID: 25843513

28. Ceccarelli M, Barthel FP, Malta TM, Sabedot TS, Salama SR, Murray BA, et al. Molecular profiling reveals biologically discrete subsets and pathways of progression in diffuse glioma. Cell. 2016; 164(3):550–63. https://doi.org/10.1016/j.cell.2015.12.028 PMID: 26824661

29. Hayward NK, Wilmott JS, Waddell N, Johansson PA, Field MA, Nones K, et al. Whole-genome landscapes of major melanoma subtypes. Nature. 2017; 545(7653):175–80. https://doi.org/10.1038/nature22071 PMID: 28467829

30. Sanchez A, Garcia HG, Jones D, Phillips R, Kondev J. Effect of Promoter Architecture on the Cell-to-Cell Variability in Gene Expression. PLOS Computational Biology. 2011; 7(3):e1001100. https://doi.org/10.1371/journal.pcbi.1001100 PMID: 21390269

31. McQuin C, Goodman A, Chernyshev V, Kamentsky L, Cimini BA, Karhohs KW, et al. CellProfiler 3.0: Next-generation image processing for biology. PLoS biology. 2018; 16(7):e2005970. https://doi.org/10.1371/journal.pbio.2005970 PMID: 29969450

32. Pachitariu M, Stringer C. Cellpose 2.0: how to train your own model. Nature Methods. 2022. https://doi.org/10.1038/s41592-022-01663-4 PMID: 36344832

33. Yang J, Peng W, Ward MO, Rundensteiner EA. Interactive hierarchical dimension ordering, spacing and filtering for exploration of high dimensional datasets. IEEE Symposium on Information Visualization 2003: IEEE Computer Society; 2003. p. 105,6,7,8,9,10,11,12.

34. Doan M, Barnes C, McQuin C, Caicedo JC, Goodman A, Carpenter AE, et al. Deepometry, a framework for applying supervised and weakly supervised deep learning to imaging cytometry. Nature Protocols. 2021; 16(7):3572–95. https://doi.org/10.1038/s41596-021-00549-7 PMID: 34145434

35. McInnes L, Healy J, Melville J. Umap: Uniform manifold approximation and projection for dimension reduction. arXiv preprint arXiv:180203426. 2018.

36. Yan W, Shao R. Transduction of a Mesenchyme-specific Gene Periostin into 293T Cells Induces Cell Invasive Activity through Epithelial-Mesenchymal Transformation *. Journal of Biological Chemistry. 2006; 281(28):19700–8. https://doi.org/10.1074/jbc.M601856200 PMID: 16702213

37. Hennig H, Rees P, Blasi T, Kamentsky L, Hung J, Dao D, et al. An open-source solution for advanced imaging flow cytometry data analysis using machine learning. Methods. 2017; 112:201–10. https://doi.org/10.1016/j.ymeth.2016.08.018 PMID: 27594698

38. Edgar RH, Tarhini A, Sander C, Sanders ME, Cook JL, Viator JA. Predicting Metastasis in Melanoma by Enumerating Circulating Tumor Cells Using Photoacoustic Flow Cytometry. Lasers Surg Med. 2021; 53(4):578–86. https://doi.org/10.1002/lsm.23286 PMID: 32557708

39. Doan M, Vorobjev I, Rees P, Filby A, Wolkenhauer O, Goldfeld AE, et al. Diagnostic Potential of Imaging Flow Cytometry. Trends in Biotechnology. 2018; 36(7):649–52. https://doi.org/10.1016/j.tibtech.2017.12.008 PMID: 29395345

40. Allemang A, Thacker R, DeMarco RA, Rodrigues MA, Pfuhler S. The 3D reconstructed skin micronucleus assay using imaging flow cytometry and deep learning: A proof-of-principle investigation. Mutation Research/Genetic Toxicology and Environmental Mutagenesis. 2021; 865:503314. https://doi.org/10.1016/j.mrgentox.2021.503314 PMID: 33865536

41. Moon KR, van Dijk D, Wang Z, Gigante S, Burkhardt DB, Chen WS, et al. Visualizing structure and transitions in high-dimensional biological data. Nature Biotechnology. 2019; 37(12):1482–92. https://doi.org/10.1038/s41587-019-0336-3 PMID: 31796933

42. Ganesh K, Basnet H, Kaygusuz Y, Laughney AM, He L, Sharma R, et al. L1CAM defines the regenerative origin of metastasis-initiating cells in colorectal cancer. Nature Cancer. 2020; 1(1):28–45. https://doi.org/10.1038/s43018-019-0006-x PMID: 32656539

43. Liu Z, Li Q, Li K, Chen L, Li W, Hou M, et al. Telomerase reverse transcriptase promotes epithelial–mesenchymal transition and stem cell-like traits in cancer cells. Oncogene. 2013; 32(36):4203–13. https://doi.org/10.1038/onc.2012.441 PMID: 23045275

44. Ding D, Xi P, Zhou J, Wang M, Cong YS. Human telomerase reverse transcriptase regulates MMP expression independently of telomerase activity via NF-κB-dependent transcription. The FASEB Journal. 2013; 27(11):4375–83.

45. Fang Y, Yuan Y, Zhang L-L, Lu J-W, Feng J-F, Hu S-N. Downregulated GBX2 gene suppresses proliferation, invasion and angiogenesis of breast cancer cells through inhibiting the Wnt/β-catenin signaling pathway. Cancer Biomarkers. 2018; 23:405–18.

46. Zhang K, Guo Y, Wang X, Zhao H, Ji Z, Cheng C, et al. WNT/β-catenin directs self-renewal symmetric cell division of hTERThigh prostate cancer stem cells. Cancer research. 2017; 77(9):2534–47.

47. Viceconte N, Dheur M-S, Majerova E, Pierreux CE, Baurain J-F, van Baren N, et al. Highly Aggressive Metastatic Melanoma Cells Unable to Maintain Telomere Length. Cell Reports. 2017; 19(12):2529–43. https://doi.org/10.1016/j.celrep.2017.05.046 PMID: 28636941

48. Robinson NJ, Schiemann WP. Telomerase in Cancer: Function, Regulation, and Clinical Translation. Cancers (Basel). 2022; 14(3).

49. Zou Y, Cong Y-s, Zhou J. Implications of telomerase reverse transcriptase in tumor metastasis. BMB reports. 2020; 53(9):458. https://doi.org/10.5483/BMBRep.2020.53.9.108 PMID: 32731912

50. Ghosh A, Saginc G, Leow SC, Khattar E, Shin EM, Yan TD, et al. Telomerase directly regulates NF-κB-dependent transcription. Nature cell biology. 2012; 14(12):1270–81.

51. Nallanthighal S, Heiserman JP, Cheon D-J. The role of the extracellular matrix in cancer stemness. Frontiers in cell and developmental biology. 2019; 7:86. https://doi.org/10.3389/fcell.2019.00086 PMID: 31334229

52. Rusinek D, Pfeifer A, Cieslicka M, Kowalska M, Pawlaczek A, Krajewska J, et al. TERT Promoter Mutations and Their Impact on Gene Expression Profile in Papillary Thyroid Carcinoma. Cancers (Basel). 2020; 12(6). https://doi.org/10.3390/cancers12061597 PMID: 32560331

53. Troyanovsky SM, Leube RE, Franke WW. Characterization of the human gene encoding cytokeratin 17 and its expression pattern. European journal of cell biology. 1992; 59(1):127–37. PMID: 1281771

54. Hu H, Xu D-h, Huang X-x, Zhu C-c, Xu J, Zhang Z-z, et al. Keratin17 promotes tumor growth and is associated with poor prognosis in gastric cancer. Journal of Cancer. 2018; 9(2):346. https://doi.org/10.7150/jca.19838 PMID: 29344281

55. Escobar-Hoyos LF, Yang J, Zhu J, Cavallo J-A, Zhai H, Burke S, et al. Keratin 17 in premalignant and malignant squamous lesions of the cervix: proteomic discovery and immunohistochemical validation as a diagnostic and prognostic biomarker. Modern Pathology. 2014; 27(4):621–30. https://doi.org/10.1038/modpathol.2013.166 PMID: 24051697

56. Regenbogen E, Mo M, Romeiser J, Shroyer ALW, Escobar-Hoyos LF, Burke S, et al. Elevated expression of keratin 17 in oropharyngeal squamous cell carcinoma is associated with decreased survival. Head & neck. 2018; 40(8):1788–98. https://doi.org/10.1002/hed.25164 PMID: 29626364

57. Sorlie T, Perou C, Tibshirani R, Aas T, Geisler S, Johnsen H. Hastie T, Eisen MB, van de Rijn M, Jeffrey SS, Thorsen T, Quist H, Matese JC, Brown PO, Botstein D, Lonning Eystein P, Borresen-Dale AL Gene expression patterns of breast carcinomas distinguish tumor subclasses with clinical implications. Proc Natl Acad Sci USA. 2001; 98:10869–74. https://doi.org/10.1073/pnas.191367098 PMID: 11553815

58. Wang Z, Zhou Q, Li A, Huang W, Cai Z, Chen W. Extracellular matrix protein 1 (ECM1) is associated with carcinogenesis potential of human bladder cancer. OncoTargets and therapy. 2019:1423–32. https://doi.org/10.2147/OTT.S191321 PMID: 30863109

59. Wang L, Yu J, Ni J, Xu X-M, Wang J, Ning H, et al. Extracellular matrix protein 1 (ECM1) is overexpressed in malignant epithelial tumors. Cancer letters. 2003; 200(1):57–67. https://doi.org/10.1016/s0304-3835(03)00350-1 PMID: 14550953

60. Raj A, van Oudenaarden A. Nature, nurture, or chance: stochastic gene expression and its consequences. Cell. 2008; 135(2):216–26. https://doi.org/10.1016/j.cell.2008.09.050 PMID: 18957198

61. Matak A, Lahiri P, Ford E, Pabst D, Kashofer K, Stellas D, et al. Stochastic phenotype switching leads to intratumor heterogeneity in human liver cancer. Hepatology. 2018; 68(3):933–48. https://doi.org/10.1002/hep.29679 PMID: 29171037

62. Deshmukh S, Saini S. Phenotypic Heterogeneity in Tumor Progression, and Its Possible Role in the Onset of Cancer. Frontiers in Genetics. 2020; 11. https://doi.org/10.3389/fgene.2020.604528 PMID: 33329751

63. Kumar N, Cramer GM, Dahaj SAZ, Sundaram B, Celli JP, Kulkarni RV. Stochastic modeling of phenotypic switching and chemoresistance in cancer cell populations. Scientific Reports. 2019; 9(1):10845. https://doi.org/10.1038/s41598-019-46926-x PMID: 31350465

64. Guinn MT, Wan Y, Levovitz S, Yang D, Rosner MR, Balázsi G. Observation and Control of Gene Expression Noise: Barrier Crossing Analogies Between Drug Resistance and Metastasis. Frontiers in Genetics. 2020; 11. https://doi.org/10.3389/fgene.2020.586726 PMID: 33193723

65. Yang S, Golkaram M, Oh S, Oh Y, Cho Y, Yoe J, et al. ETV4 is a mechanical transducer linking cell crowding dynamics to lineage specification. Nature Cell Biology. 2024. https://doi.org/10.1038/s41556-024-01415-w PMID: 38702503

66. Schraivogel D, Kuhn TM, Rauscher B, Rodríguez-Martínez M, Paulsen M, Owsley K, et al. High-speed fluorescence image–enabled cell sorting. Science. 2022; 375(6578):315–20. https://doi.org/10.1126/science.abj3013 PMID: 35050652

67. Salek M, Li N, Chou H-P, Saini K, Jovic A, Jacobs KB, et al. COSMOS: a platform for real-time morphology-based, label-free cell sorting using deep learning. Communications Biology. 2023; 6(1):971. https://doi.org/10.1038/s42003-023-05325-9 PMID: 37740030

68. Mudla A, Jiang Y, Arimoto KI, Xu B, Rajesh A, Ryan AP, et al. Cell-cycle-gated feedback control mediates desensitization to interferon stimulation. Elife. 2020; 9. https://doi.org/10.7554/eLife.58825 PMID: 32945770

69. Ogrodnik M, Salmonowicz H, Brown R, Turkowska J, Średniawa W, Pattabiraman S, et al. Dynamic JUNQ inclusion bodies are asymmetrically inherited in mammalian cell lines through the asymmetric partitioning of vimentin. Proceedings of the National Academy of Sciences. 2014; 111(22):8049–54. https://doi.org/10.1073/pnas.1324035111 PMID: 24843142

70. Zabary Y, Zaritsky A. A MATLAB Pipeline for Spatiotemporal Quantification of Monolayer Cell Migration. Bioimage Data Analysis Workflows–Advanced Components and Methods: Springer; 2022. p. 175–206.

71. Schneider CA, Rasband WS, Eliceiri KW. NIH Image to ImageJ: 25 years of image analysis. Nature Methods. 2012; 9(7):671–5. https://doi.org/10.1038/nmeth.2089 PMID: 22930834

72. Stirling DR, Swain-Bowden MJ, Lucas AM, Carpenter AE, Cimini BA, Goodman A. CellProfiler 4: improvements in speed, utility and usability. BMC Bioinformatics. 2021; 22(1):433. https://doi.org/10.1186/s12859-021-04344-9 PMID: 34507520